JACS
JOURNAL OF THE AMERICAN CHEMICAL SOCIETY

Article

pubs.acs.org/JACS

"Manganese Extraction" Strategy Enables Tumor-Sensitive Biodegradability and Theranostics of Nanoparticles

Luodan Yu,[†,‡] Yu Chen,[*,†] Meiying Wu,[†,‡] Xiaojun Cai,[†,‡] Heliang Yao,[†] Linlin Zhang,[†] Hangrong Chen,[*,†] and Jianlin Shi[*,†]

[†]The State Key Lab of High Performance Ceramics and Superfine Microstructures, Shanghai Institute of Ceramics, Chinese Academy of Sciences, Shanghai 200050, P. R. China

[‡]University of Chinese Academy of Sciences, Beijing 100049, P.R. China

Supporting Information

ABSTRACT: Biodegradability of inorganic nanoparticles is one of the most critical issues in their further clinical translations. In this work, a novel "metal ion-doping" approach has been developed to endow inorganic mesoporous silica-based nanoparticles with tumor-sensitive biodegradation and theranostic functions, simply by topological transformation of mesoporous silica to metal-doped composite nanoformulations. "Manganese extraction" sensitive to tumor microenvironment was enabled in manganese-doped hollow mesoporous silica nanoparticles (designated as Mn-HMSNs) to fast promote the disintegration and biodegradation of Mn-HMSNs, further accelerating the breakage of Si−O−Si bonds within the framework. The fast biodegradation of Mn-HMSNs sensitive to mild acidic and reducing microenvironment of tumor resulted in much accelerated anticancer drug releasing and enhanced T_1-weighted magnetic resonance imaging of tumor. A high tumor-inhibition effect was simultaneously achieved by anticancer drug delivery mediated by PEGylated Mn-HMSNs, and the high biocompatibility of composite nanosystems was systematically demonstrated in vivo. This is the first demonstration of biodegradable inorganic mesoporous nanosystems with specific biodegradation behavior sensitive to tumor microenvironment, which also provides a feasible approach to realize the on-demand biodegradation of inorganic nanomaterials simply by "metal ion-doping" strategy, paving the way to solve the critical low-biodegradation issue of inorganic drug carriers.

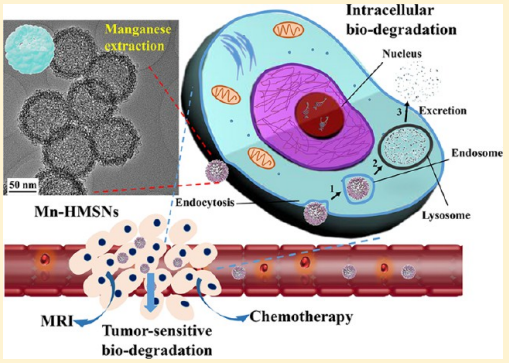

1. INTRODUCTION

The fast development of nanomedicine and nanobiotechnology has catalyzed the fabrication of various nanosystems with abundant nanostructures and compositions for biomedicine, which can be mainly divided into three typical categories: organic, inorganic, and organic−inorganic hybridized nanosystems.[1,2] Especially, inorganic nanoparticles (NPs) have attracted great attention from the scientific community in the past decades, on account of their physiological stability, easy functionalization, and other unique physiochemical properties. The employment of inorganic NPs as drug delivery systems (DDSs)[3−8] is of intense interest owing to their high biosafety and delivery efficiency, satisfactory biocompatibility, controllable drug-releasing profile, and potential targeting capability. Various inorganic nanosystems have been developed as DDSs,[9−11] such as TiO_2,[12] Au,[13−17] Ag,[18] carbon nanotubes,[19−22] Fe_3O_4,[18,23−25] quantum dots,[26] etc. However, the clinical translation of these NPs is still highly rare because of the lack of clear evidence and the limited data to prove their biosafety, especially the critical issue of low biodegradability of these inorganic nanosystems.[27]

Mesoporous silica NPs (MSNs), as one of the most representative inorganic nanosystems,[28−32] have been extensively explored for drug delivery,[4,33−36] molecular imaging,[15,37] biosensing,[31,33,38] and synergistic cancer therapy.[10,39−46] However, the physiologically inert nature of −Si−O−Si− framework makes it difficult to biodegrade in physiological conditions.[47,48] The reluctant biodegradation of MSNs may lead to the accumulation of the carriers within the body, leading to a potential biosafety issue. However, optimizing the biodegradation of MSNs has not been effectively realized to date, which has become one of the most critical obstacles in their further clinical translations. To promote the biodegradation of solid silica without mesopores, Trogler et al. developed a kind of silica NPs with improved biodegradability by doping iron(III) into the framework.[47] However, the fabricated silica NPs were nonmesoporous and severely aggregated with each other, thus nonapplicable for further biomedical applications such as drug delivery. Li et al. reported organic−inorganic hybrid SiO_2-drug composite NPs, which were constructed by encapsulating drug molecules into the framework of SiO_2 carrier during the growth of NPs. The drug release from the SiO_2 NPs simultaneously triggered the carrier decomposition.[49] Nevertheless, this synthetic method toward SiO_2-drug composite is not a general protocol for carrier-drug formation

Received: April 27, 2016
Published: July 21, 2016

ACS Publications © 2016 American Chemical Society

DOI: 10.1021/jacs.6b04299
J. Am. Chem. Soc. 2016, 138, 9881−9894

and the synthetic alkaline condition will potentially cause the denaturing of drug molecules. Therefore, the presently reported optimization approaches of silica-based biodegradation will either cause the aggregation of NPs or potentially change the pharmacological nature of drugs. It still remains a big challenge to regulate the biodegradability of silica-based nanocarriers, especially in the ones with well-defined mesopores in the carrier matrix.

Herein, a simple and highly versatile "metal ion-doping" (MI-D) approach has been successfully developed to concurrently enable tumor microenvironment-triggered biodegradation and theranostic functions of MSNs. Via this MI-D strategy, transition metal manganese (Mn) was directly doped into the framework of MSNs to change the intrinsic biological nature of MSNs, especially the biodegradation behavior. Manganese was chosen based on the fact that Mn is one of the necessary elements in human bodies for metabolism, and the biological system can efficiently control its uptake and excretion, showing low toxicity and high biosafety.[50] Especially, the introduced manganese ions within the framework can act as the contrast agent for T_1-weighted magnetic resonance imaging (MRI) due to the paramagnetic nature of manganese ions.[51−58] Recent research has demonstrated that −Mn−O− bonds could respond to a tumor's microenvironment such as reducing or acidic conditions.[57,59−61] Based on these results, we assumed that the introduction of −Mn−O− bonds into the −Si−O−Si− framework of MSNs could change the biodegradation nature of MSNs and, more importantly, make the degradation sensitive to the special intratumoral microenvironment. This research has successfully verified our assumption and shows the unique "manganese extraction" performance responsive to a tumor's microenvironment and the corresponding biological behavior of manganese-doped hollow MSNs (designated as Mn-HMSNs) for drug delivery. "Manganese extraction" refers to the breaking-up and subsequent releasing of Mn ions from the framework of Mn-doped HMSNs under either mild acidic or reducing microenvironment. As a result, manganese oxide dissolves from the framework of Mn-HMSNs, promoting the disintegration and biodegradation of Mn-HMSNs. On one hand, the formed Mn−O bonds within the framework can fast biodegrade in the mild reducing or acidic microenvironment based on the intrinsic breaking-up capability of the Mn−O bond under these two conditions. It is noted that the breaking-up of the Mn−O bond and subsequent releasing of manganese ions from the framework can generate abundant defects within the framework and further induce/accelerate the framework biodegradation including the cleavage of Si−O bonds. On the other hand, the "manganese extraction" and fast biodegradation of MSNs will significantly enhance the T_1-weighted MRI performance for efficient tumor-diagnostic imaging thanks to the Mn^{2+} releasing. Last but not least, the well-defined mesostructure of Mn-HMSNs could act as the reservoirs for efficient drug delivery, as systematically demonstrated both in vitro and in vivo. The high histocompatibility of Mn-HMSNs was also demonstrated in vivo.

In brief, the specific novelties of this work are (i) successful fabrication of hollow mesoporous silica-based composite nanostructures with much enhanced transitional metal-doping amount within the framework, (ii) facile regulation of the biodegradability and theranostic functions of inorganic nanosystems with tumor sensitivity simply by transitional metal-ions doping into the framework of inorganic MSNs, and (iii) first detailed probing of structural evolutions of Mn-doped mesoporous silica nanosystems during the tumor-sensitive biodegradation process and the corresponding biodegradation-induced stimuli-responsive drug releasing and tumor-sensitive T_1-weighted MRI performances.

2. EXPERIMENTAL SECTION

2.1. Chemicals and Regents. Tetraethyl orthosilicate (TEOS), triethanolamine (TEA), ethanol, and methyl alcohol were obtained from Sinopharm Chemical Reagent Co. Cetyltrimethylammonium chloride (CTAC), disodium maleate, manganese(II) sulfate monohydrate ($MnSO_4·H_2O$), and glutathione (GSH) were purchased from Sigma-Aldrich. Antitumor chemotherapeutic doxorubicin (DOX) was obtained from Beijing HuaFeng United Technology Co., Ltd. Methoxy PEG Silane, (M_w = 2000, M-SLN-2000) was ordered from JenKem Technology. Simulated body fluid (SBF) was prepared by using the following chemicals, including sodium chloride (NaCl), sodium bicarbonate ($NaHCO_3$), potassium chloride (KCl), potassium hydrogen phosphate trihydrate ($K_2HPO_4·3H_2O$), magnesium chloride hexahydrate ($MgCl_2·6H_2O$), calcium chloride ($CaCl_2$), sodium sulfate (Na_2SO_4), and trimethylolaminomethane [Tris: $(HOCH_2)_3CNH_2$], which were purchased from Sinopharm Chemical Reagent Co. All chemicals were used without further purification. Ultrapure water was used in the preparation of SBF, while deionized water was used in the other experiments.

2.2. Synthesis of Manganese-Doped Hollow Mesoporous Silica NPs (Mn-HMSNs). Synthesis of Mn-HMSNs was divided into two steps, including synthesis of MSNs and subsequent doping Mn component into MSN's framework. First, MSNs were prepared via a typical sol−gel procedure by using surfactants as pore-making agents. Cetyltrimethylammonium chloride (CTAC, 2 g) and triethanolamine (TEA, 0.02 g) were diluted in turn with 20 mL of water at 80 °C under magnetic stirring for 20 min. Then, 1.5 mL of tetraethylorthosilicate (TEOS) was added dropwise into the solution, and the mixture was stirred for another 4 h at 80 °C. The product was collected by centrifugation (18000 r/min, 15 min) and washed several times with ethanol and water to remove the residual precursors and reactants. Finally, the surfactants (CTAC) of MSNs were extracted by stirring in a solution of sodium chloride (NaCl) in methanol (8 mg/mL, 12 h stirring) for three rounds. For Mn doping, the as-synthesized MSNs were initially dispersed into 10 mL of water. Then, a mixture solution (10 mL) of $MnSO_4·H_2O$ (8 mg/mL) and disodium maleate (10 mg/mL) was added into MSNs aqueous solution dropwise under stirring. The mixture was treated under hydrothermal condition at 180 °C for 12 h. The product was collected by centrifugation and washed with ethanol and water several times to remove the residual reactants.

2.3. PEGylation of Mn-HMSNs (PEG/Mn-HMSNs). Typically, Mn-HMSNs (10 mg) were dispersed into M-SLN-2000 ethanol solution (100 mL, 0.5 mg/mL) under magnetic stirring at 60 °C. After 24 h reaction, PEGylated Mn-HMSNs were collected by centrifugation. To remove the residual M-SLN-2000, the product was rinsed with ethanol and deionized water several times.

2.4. DOX Loading and in Vitro Release of DOX from DOX-Loaded PEG/Mn-HMSNs. PEG/Mn-HMSNs (5 mg) were dispersed into doxorubicin (DOX) PBS solution (20 mL, 0.5 mg/mL) under magnetic stirring in dark conditions. DOX-loaded PEG/Mn-HMSNs were collected by centrifugation after 24 h stirring, and the supernatant solution was collected to evaluate the DOX-loading efficiency. The residual DOX concentration of the supernatant solution was measured by UV−vis spectra at a wavelength of 480 nm. To assess in vitro release of DOX, 5 mg of DOX-loaded PEG/Mn-HMSNs was encapsulated into a dialysis bag and put into 30 mL of SBF solutions at different GSH concentrations ([GSH] = 0, 5.0, and 10.0 mM) or SBF solutions with different pHs (7.4 and 5.0). Then, the releasing process was performed in a shaking table at a shaking speed of 142 rpm at 37 °C, and the released DOX was monitored by UV−vis spectra at a time-course manner.

2.5. Characterization. Transmission electron microscopy (TEM) micrographs were taken to observe the morphology of the nanoparticles on a JEM-2100F electron microscope operated at 200

DOI: 10.1021/jacs.6b04299
J. Am. Chem. Soc. 2016, 138, 9881−9894

Scheme 1. Schematic Illustration of Transport of PEG/Mn-HMSNs within Blood Vessel, Subsequent Intracellular Delivery, Biodegradation and Enhanced Theranostic Functions by "Manganese Extraction" of PEG/Mn-HMSNs and Releasing of Mn(II) Component Intracellularly

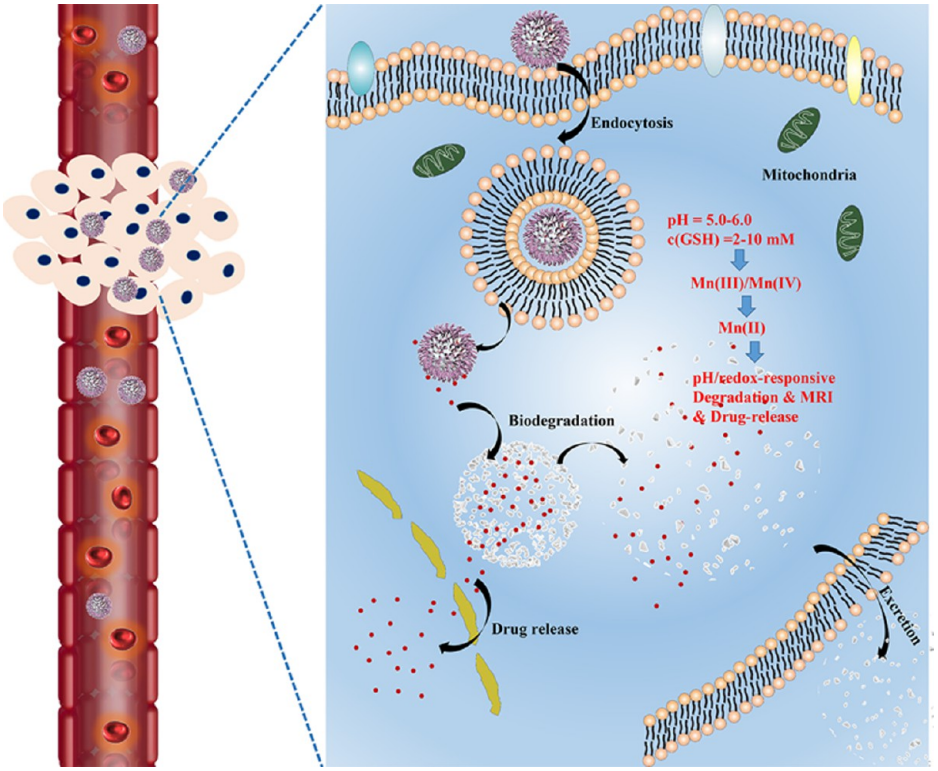

kV. Energy dispersive X-ray spectroscopy (EDS) was performed simultaneously on JEM-2100F electron microscope. X-ray photoelectron spectroscopy (XPS) was acquired to observe the different valence states of doped manganese component on an ESCALAB 250Xi X-ray photoelectron spectroscopy. Scanning electron microscope (SEM) images and element mapping images were obtained to intuitively display the elements distribution of Mn-HMSNs on a field-emission Magellan 400 microscope (FEI Co.). The N_2 adsorption−desorption isotherm and corresponding pore-size distribution were tested to characterize the mesoporous structure of Mn-HMSNs on a Micrometitics Tristar 3000 system. Dynamic light scattering (DLS) was measured to determine the hydrodynamic particle sizes of Mn-HMSNs on a Zetasizer Nanoseries (Nano ZS90). The phases of Mn-HMSNs were determined by X-ray diffraction (XRD Bruker D8 Focus) with a monochromatized source of Cu Ka1 radiation (l = 0.15405 nm) at 1.6 kW (40 kV, 40 mA).The ^{29}Si solid-state MAS NMR spectra were tested on AVANCE III HD 500 MHz solid NMR spectrometer operating at 1H Larmor frequency of 500 MHz.

2.6. Cell Culture and Animals. *2.6.1. Cell Culture.* Hep G2 cells and 4T1 cells were cultured in Dulbecco's modified Eagle medium (DMEM) containing 10% fetal bovine serum (FBS), 100 U/mL streptomycin and 100 U/mL penicillin. The cells were cultured at 37 °C in a humidity incubator supplied with 5% CO_2. For all experiments, cells were collected by using 0.25% trypsin and recultured in fresh medium for subsequent experiment.

2.6.2. Animals. Four-week old female BALB/c nude mice (18−20 g) and four-week old female Kunming mice (20−22 g) were purchased from Shanghai Experimental Animal Center (Shanghai). All in vivo experiments were performed under the guideline approved by Shanghai Institute of Biochemistry and Cell Biology, Chinese Academy of Sciences.

2.7. Degradation Experiment in Vitro. In vitro degradation profiles and microstructure evolutions of Mn-HMSNs were assessed by two typical approaches. One was detecting the accumulated degradation content of Mn and Si by ICP-OES, and the other was directly observing the time-dependent structural evolution of Mn-HMSNs by TEM during the degradation evaluation.

Typically, PEG/Mn-HMSNs (or PEG/MSNs) were added into SBF solution (pH. 7.4) without or with GSH (5.0 mM and 10.0 mM), respectively. To investigate the pH influence on biodegradation, SBF solution with different pHs were adopted (pH 7.4 and 5.0). It was noted that all of the evaluation was based on the concentration of 0.1 mg/mL PEG/Mn-HMSNs. The testing solution was put into a water bath at 37 °C under magnetic stirring slowly (250 rpm). At given time, a small amount of degradation solution was taken out for ICP-OES test and TEM observations.

2.8. Intracellular Degradation Behavior Observation by bio-TEM. To study the degradation process of Mn-HMSNs in live cells, 4T1 cells were cultured with Mn-HMSNs-dispersed DMEM medium (the concentration of Mn-HMSNs was 100 μg/mL) in culture conditions (5% CO_2, 37 °C) for 1, 2, 3, and 7 d, respectively. The cells were harvested by cells scraper to make sure the cells maintained their natural morphology. Thereafter, the collected cells were fixed and put onto copper grids for further bio-TEM observation according to a standard sample preparation procedure of bio-TEM.

2.9. In Vitro Cytotoxicity. The typical 3-[4, 5-dimethylthiazol-2-yl]-2,5 diphenyltetrazolium bromide (MTT) reduction assay was conducted to evaluate the in vitro cytotoxicity. To assess the cytotoxicity of DOX-loaded PEG/Mn-HMSNs and DOX-loaded PEG/MSNs against cancer cells, Hep G2 cells were seeded in 96-well plates (around 2 × 10^3 per well) and cultured in culture conditions (5% CO2, 37 °C) for 24 h. Free DOX, DOX-loaded PEG/Mn-HMSNs, and DOX-loaded PEG/MSNs were dispersed into the culture media (DMEM) at the equivalent DOX concentrations, and the concentrations of DOX were 0, 0.16, 0.31, 0.63, 1.25, 2.5, 5, 10, 20, and 40 μg/mL. The cells were then incubated in favorable culture conditions for another 24 h. Finally, the media was removed and 100 μL of MTT solution (MTT dissolved in DMEM at a concentration of 0.5 mg/mL) was added into each well. Then, the 96-well plates were incubated at 37 °C with 5% CO_2 for another 4 h. The solution was then removed, and 100 μL of dimethyl sulfoxide (DMSO) per well

DOI: 10.1021/jacs.6b04299
J. Am. Chem. Soc. 2016, 138, 9881−9894

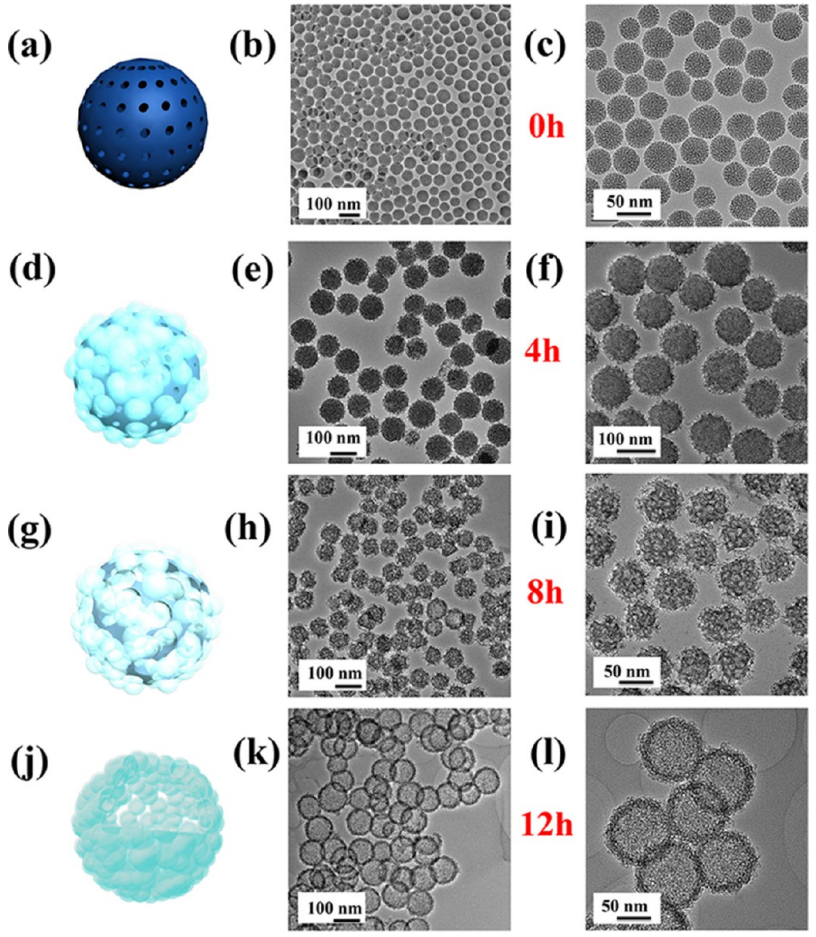

Figure 1. Schematic illustrations and TEM images of (a–c) MSNs and Mn-HMSNs after hydrothermal treatments for (d–f) 4, (g–i) 8, and (j–l) 12 h at varied TEM magnifications.

was added, and the absorbance of every well was monitored at the featured wavelength (490 nm) by a microplate reader (Bio-TekELx800). The percentage of cell viability of the experimental group compared to the control cells was used to express the cytotoxicity.

The in vitro cytotoxicity of blank PEG/Mn-MSNs NPs was also assessed by the similar MTT assay. The concentrations of PEG/Mn-MSNs were 0, 50, 100, 200, and 400 μg/mL.

2.10. CLSM Observations of the Intracellular Release of DOX from DOX-Loaded PEG/Mn-HMSNs. For confocal laser scanning microscopy (CLSM) observation, Hep G2 cells were seeded in a CLSM-specific dish with a cell density of 60%–80%. DOX-loaded PEG/Mn-HMSNs were dispersed into DMEM cell-culture media. The cells were then cultured with DOX-NPs-dispersed DMEM media ([DOX] = 10 μg/mL) at 37 °C in a humidity incubator for different time intervals (4 and 8 h). Then, the cells were washed with PBS (phosphate buffer saline) three times and stained by DAPI (4′, 6-diamidino-2-phenylindole). A CLSM apparatus (FV 1000, Olympus, Japan) was used to record the fluorescence images of cells.

2.11. In Vivo Biocompatibility Assay. To study the in vivo histocompatibility, the healthy four-week female Kunming mice were used in this work. These mice were injected with PEG/Mn-HMSNs-dispersed saline solution via tail intravenous administration at the doses of 5, 10, and 20 mg/kg. In addition, the mice receiving saline were employed as the control group. The behaviors of mice which are responsible for toxic effects were observed every 2 days, including feeding, weights, etc. The mice were sacrificed and the tissue and blood samples were harvested on the 30th day postinjection.

2.12. Establishment of Tumor Xenograft on Nude Mice. Four-week old female BALB/c nude mice (18–20 g) were purchased from Shanghai Experimental Animal Center (Shanghai). Hep G2 cells with a density of 1×10^7 were incubated in culture dishes for establishing tumor models. The cells were collected by centrifugation (3000 r/min, 3 min) and redispersed in 3 mL of a PBS solution. The tumor xenograft on nude mice was established via subcutaneous injection on the back of nude mice with 100 μL of Hep G2 cells PBS solution per mouse. The tumors grew obviously on the fifth day after postinjection of tumor cells.

2.13. In Vivo Antitumor Efficiency of DOX-PEG/Mn-HMSNs. To assess the tumor-growth inhibition effect by different treatments, the nude mice with transplanted tumors were intravenously injected with free-DOX saline and DOX-PEG/Mn-HMSNs saline at low equivalent DOX dose of 2.5 mg/kg (n = 5 in each group), and the group treated with pure saline was employed as the control group. The tumors volume was monitored every 2 days after chemotherapeutic administration.

3. RESULTS AND DISCUSSION

3.1. Design, Synthesis, and Characterization of Mn-HMSNs. This research provides the first demonstration that the biodegradation behavior of mesoporous silica can be regulated to become sensitive to tumor microenvironment simply by manganese doping in HMSN's framework based on the specific "manganese extraction" principle under mild acidic and/or reducing conditions. Importantly, such a unique biodegradation behavior enables intelligent tumor microenvironment-responsive diagnostic imaging and anticancer drug releasing. As shown in Scheme 1, sub-100 nm PEGylated Mn-doped HMSNs (PEG/Mn-HMSNs) can freely transport within blood vessel, and accumulate into tumor tissue via the typical enhanced

DOI: 10.1021/jacs.6b04299
J. Am. Chem. Soc. 2016, 138, 9881–9894

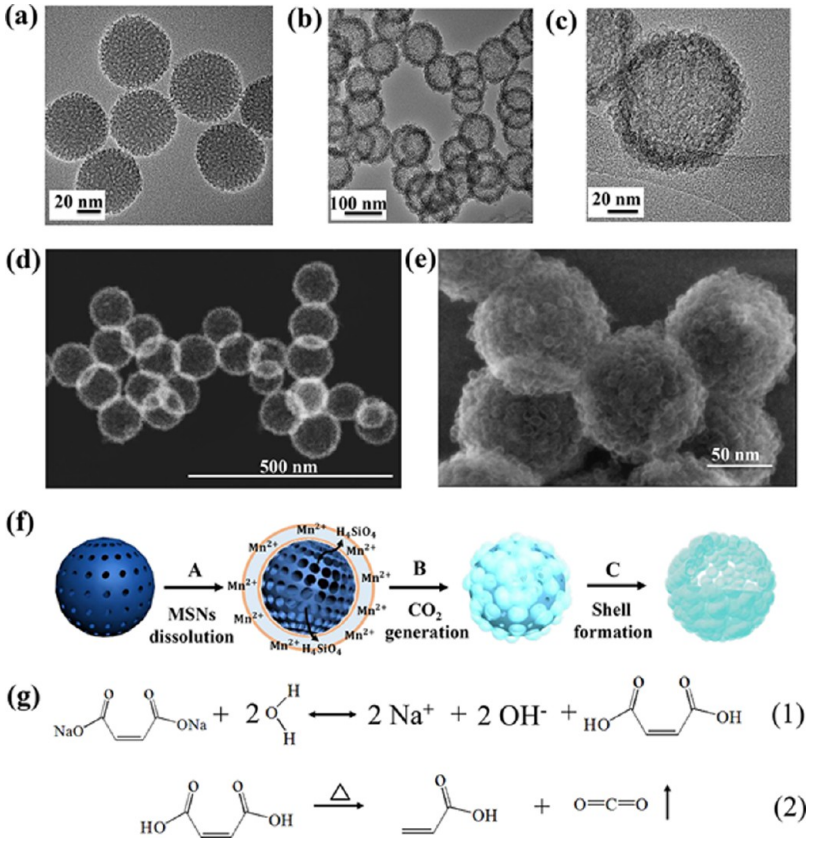

Figure 2. TEM images of (a) MSNs and (b and c) Mn-HMSNs. (d) Dark-field STEM image and (e) SEM image of Mn-HMSNs. (f) Schematic illustration of the formation mechanism of Mn-HMSNs: MSNs dissolution to release H_4SiO_4 (step A), decomposition of carboxylate species to generate CO_2 nanobubbles (step B) and chemical reaction between Mn^{2+} and H_4SiO_4 species forming Mn-HMSNs solid nanospheres onto the surface of HMSNs, finally forming hollow nanosphere-stacked Mn-HMSNs (step C). (g) Reactions of disodium maleate with water enabling the Mn-HMSNs' formation: (1) producing gentle alkalescent solution environment and further promoting MSNs hydrolysis to H_4SiO_4 and (2) generating CO_2 serving as gas−liquid template.

permeability and retention (EPR) effect. PEG/Mn-HMSNs can be easily endocytosized into tumor tissue, and either mild acidic or reducing microenvironment will trigger the "manganese extraction" and the subsequent biodegradation of PEG/Mn-HMSNs. Simultaneously, the "manganese extraction" from PEG/Mn-HMSNs and dissolving of Mn(II) can trigger the quick releasing of loaded anticancer drugs and enhance the contrast-enhanced T_1-weighted MR imaging. Based on this strategy, biodegradation and enhanced theranostic functions can be achieved concurrently, which means that such a PEG/Mn-HMSNs-based nanoplatform will be highly promising in solving the critical issues of biodegradation and theranostic functions of traditional silica-based inorganic nanosystems.

Herein, a simple but versatile approach has been developed to fabricate Mn-doped HMSNs by in situ topological transformation of monodispersed MSNs into Mn-HMSNs under hydrothermal condition, i.e., the Mn doping and formation of hollow nanostructure are achieved simultaneously. Monodispersed MSNs (Figure 1a−c) with well-defined mesoporous structure were initially synthesized by using cetyltrimethylammonium chloride (CTAC) surfactant as the structure-directing agent and triethanolamine (TEA) as the alkaline catalyst via a typical sol−gel process.[3,28,29,62−64] As-synthesized MSNs of about 60−70 nm in particle diameter were then dispersed into a solution containing Mn precursors ($MnSO_4·H_2O$). Under high-temperature hydrothermal treatment, the inner part of MSNs dissolved to release silica oligomers, which would interact with Mn precursors to form Mn-doped silica layers onto the surface of MSNs. The dissolving of the silica core generated a hollow nanostructure, and the shell of MSNs acted as the growth sites for Mn-doped mesoporous silica layer, which was resistant to high-temperature etching. TEM was employed to observe the structure evolution during such a dissolving and regrowth process. After hydrothermal treatment of MSNs in Mn precursor-containing solution for 4 h (Figure 1d−f), the surface of MSNs became rough and large voids were created in the inner part of MSNs, which became clearer after 8 h treatment (Figure 1g−i). After the hydrothermal treatment for 12 h, Mn-HMSNs were obtained with mesoporous shells and hollow interiors (Figure 1j−l).

The TEM image at high magnification shows that the initial mesoporous structure of MSNs (Figure 2a) has transformed into large amount of small nanobubbles on the surface of Mn-HMSNs (Figure 2b,c). The hollow nanostructure of Mn-HMSNs was further revealed by dark-field scanning TEM (STEM, Figure 2d), and the formation of many small nanobubbles can be clearly observed in the SEM image (Figure 2e). The diameter of the obtained Mn-HMSNs is around 80 nm, as shown in TEM image (Figure 2b,c). Further surface PEGylation of Mn-HMSNs could guarantee their high dispersity both in deionized water and saline with the average particle size of 141.0 and 187.0 nm (Figure S1), respectively, determined by the dynamic light scattering (DLS) tests.

DOI: 10.1021/jacs.6b04299
J. Am. Chem. Soc. 2016, 138, 9881−9894

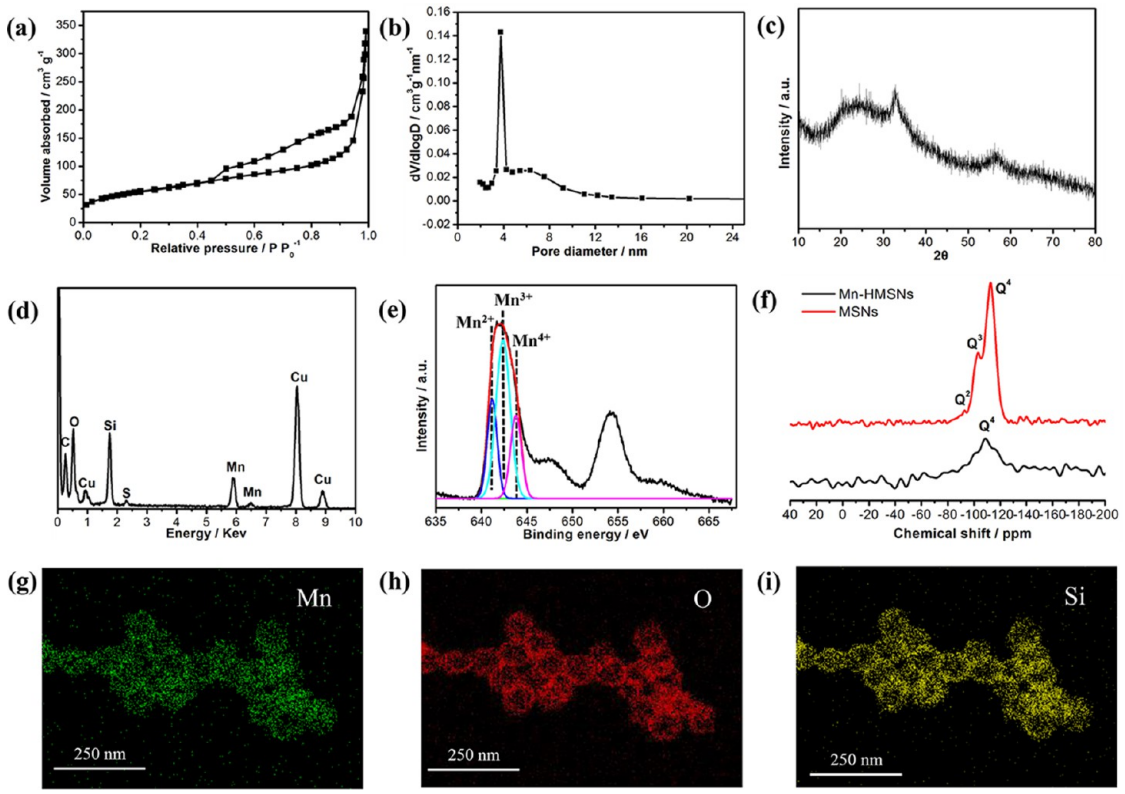

Figure 3. (a) N_2 absorption−desorption isotherm and (b) corresponding pore-size distribution of Mn-HMSNs. (c) XRD pattern, (d) EDS spectrum, and (e) XPS spectrum of Mn-HMSNs. (f) ^{29}Si solid-state MAS NMR spectra of MSNs and Mn-HMSNs. EDS elemental mapping of (g) Mn, (h) O, and (i) Si of Mn-HMSNs.

A specific gas−liquid interface-templating mechanism is here proposed to demonstrate the formation of these unique Mn-HMSNs NPs with small nanocapsules stacking on the shell (Figure 2f). First, in a gentle alkalescent solution produced by adding disodium maleate (Figure 2g, reaction **1**), a small amount of silica from the inner part of MSNs was hydrolyzed to H_4SiO_4 under hydrothermal condition.[65−67] Simultaneously, active sites were generated on the surface of MSNs to adsorb Mn^{2+} and carboxylate species via disodium maleate decomposition in the solution (Figure 2f, step A). The absorption of Mn^{2+} decreased the activation energy for the chemical decomposition of carboxylate. Subsequently, carboxylate species decomposed into CO_2 and other gaseous species under hydrothermal treatment (Figure 2f, step B, and g, reaction 2). Second, the reaction between Mn^{2+} and H_4SiO_4 species resulted in Mn-doped silica deposition on the gas−liquid interface, forming solid nanospheres on the surface of MSNs (Figure 2f, step B; Figure 1g−i). Finally, the same deposition and growth procedures continued to generate hollow nanosphere-stacked structure with large hollow interior (Figure 2f, step C; Figure 1 j−l).

As-synthesized Mn-HMSNs exhibit well-defined mesoporous structure, as demonstrated by N_2 absorption−desorption isotherm (Figure 3a) and corresponding pore-size distribution (Figure 3b). The surface area, pore volume and average pore size of Mn-HMSNs are 222.0 m^2/g, 0.53 cm^3/g, and 3.8 nm, respectively. X-ray diffraction (XRD) pattern (Figure 3c) of Mn-HMSNs shows several broadened peaks of $Mn_x(SiO_4)_y$, indicating the covalent bonding of Mn species within silica framework. The major peaks of the XRD pattern can be indexed to braunite-1Q ($Mn^{2+}Mn^{3+}{}_6SiO_{12}$, JCPDS no. 33-0904) phase.[65] The Mn-doping amount is nearly 9.4% (mass ratio), as demonstrated by energy-dispersive spectrum (EDS) test (Figure 3d).

X-ray photoelectron spectroscopy (XPS) (Figure 3e) of Mn-HMSNs was used to analyze the valence state of Mn. The main peak of Mn $2p_{3/2}$ could be divided into three characteristic peaks at 641, 642, and 644 eV, which were indexed to Mn^{2+}, Mn^{3+}, and Mn^{4+} species with the amount of 25%, 50%, and 25%, respectively. Furthermore, ^{29}Si solid-state MAS NMR of Mn-HMSNs was conducted to show the bond linkage. It can be found that distinctive peaks at −110 (Q^4, $Si(OSi)_4$) and −100 ppm (Q^3, $Si(OSi)_3(OH)$) appearing in the MSNs spectrum become much weaker after Mn doping, which is considered to be the result of Mn substitution for Si within the framework, forming abundant Mn−O−Si bonds. To further show the successful Mn doping, element mapping of Mn-HMSNs was conducted, which showed that Mn component was uniformly distributed within the shell of Mn-HMSNs (Figure 3g−i). The unique hollow nanostructure was also clearly demonstrated in Mn, O and Si mappings as shown in signal intensity variations of elements.

3.2. Biodegradation of Mn-HMSNs Sensitive to Tumor Microenvironment. It has been well-demonstrated that Mn−O bonds are sensitive to mild acidic and reducing microenvironment to enable the "manganese extraction", which is fortunately the characteristic feature of tumor microenvironment compared to normal tissues.[57,59−61] It is expected that the presence of Mn−O bonds within the framework of Mn-HMSNs can be disintegrated in such a condition, which can further accelerate the biodegradation of silica component. To imitate the tumor microenvironment, simulated body fluid

DOI: 10.1021/jacs.6b04299
J. Am. Chem. Soc. 2016, 138, 9881−9894

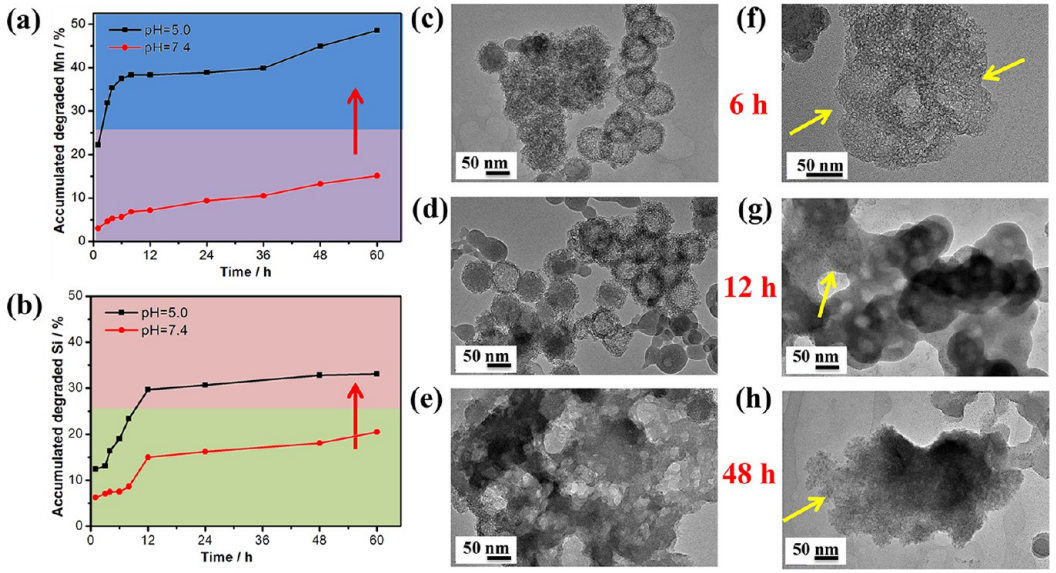

Figure 4. Accumulated releasing profiles of biodegraded (a) Mn and (b) Si components in SBF at varied pHs. TEM images of Mn-HMSNs after biodegradation for (c, f) 6, (d, g) 12, and (e, h) 48 h in SBF solutions at (c, d, and e) pH.7.4 and (f, g, and h) 5.0.

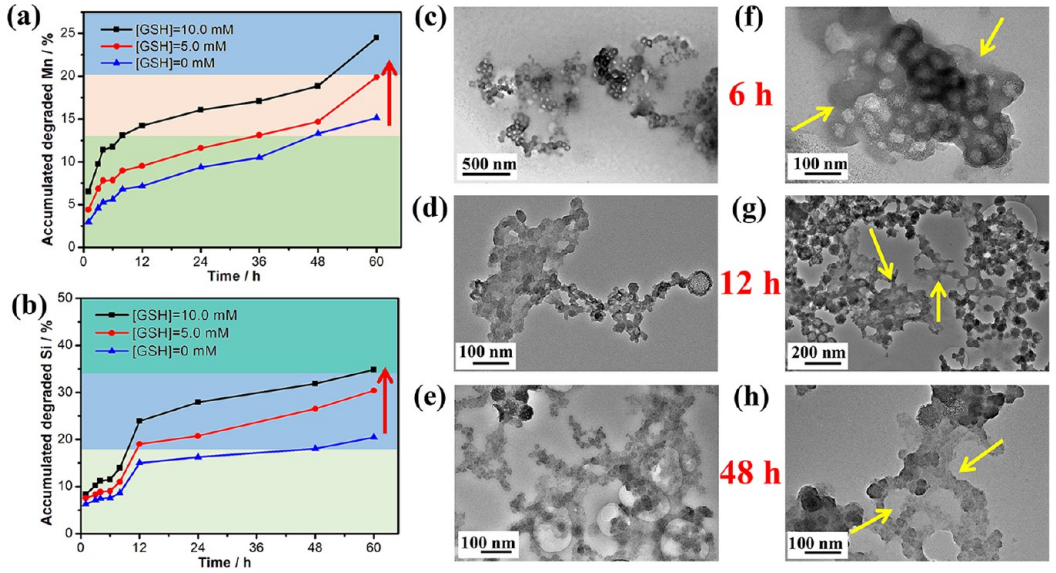

Figure 5. Accumulated releasing profiles of (a) Mn and (b) Si elements in SBF at varied GSH concentrations under neutral condition ([GSH] = 0, 5.0, and 10.0 mM). TEM images of Mn-HMSNs after biodegradation for (c, f) 6, (d, g) 12, and (e, h) 48 h in SBF solutions at GSH concentrations of (c, d, and e) 5.0 and (f, g, and h) 10.0 mM.

(SBF) solutions with varied pHs and GSH concentrations were adopted for detailed biodegradation evaluations. Mn-HMSNs were directly immersed into SBF solutions, and the degradation process was monitored by ICP tests and TEM observations. SBF solutions with low pH (5.0) and GSH (5.0 mM and 10.0 mM) were used to mimic the acidic and reducing condition of the intrinsic tumor microenvironment, respectively. The pH of tumor extracellular microenvironment is about 7.2−6.5 depending on the type and stage of tumor while that of intracellular early endosome and lysosome reaches 6.2−5.0. The pH.5.0 was adopted here as a paradigm to show the acidity-responsive biodegradation and theranostic functions of Mn-doped HMSNs. As shown in Figure 4a, the releasing of Mn from Mn-HMSNs is substantially accelerated under mild acidic condition (pH.5.0) compared to that in neutral SBF. Importantly, the fast releasing of Mn from Mn-HMSNs has accelerated the releasing of Si from the carrier, as shown in Figure 4b. TEM image was used to directly observe the structural evolution of Mn-HMSNs during biodegradation (Figure 4c−h). It can be found that the framework has undergone significant change only in 6 h incubation within acidic SBF solution (Figure 4f), and the nano/meso-structure of Mn-HMSNs was almost completely destroyed only in 48 h of biodegradation (Figure 4h). Comparatively, the hollow structure of Mn-HMSNs still kept intact to a large extent in the same period of biodegradation under neutral condition. The Si/Mn releasing profiles and TEM observations provide the direct evidence that the breakup of Mn−O bonds in acidic condition promotes the fast biodegradation of −Si−O−Si− bonds afterward.

As extensively reported, tumor tissue and tumor cytosol are commonly featured with reducing microenvironment with

DOI: 10.1021/jacs.6b04299
J. Am. Chem. Soc. 2016, 138, 9881−9894

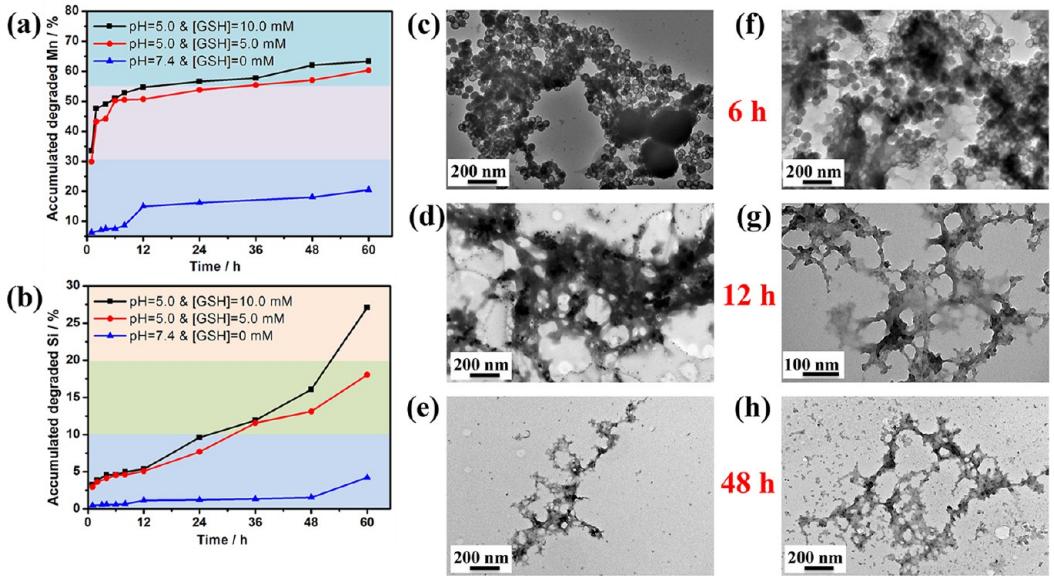

Figure 6. Accumulated releasing profiles of (a) Mn and (b) Si elements in SBF at different GSH concentrations (5.0 and 10. mM) under acidic condition (pH.5.0). TEM image showing the structural evolution of Mn-HMSNs after the biodegradation at the GSH concentration of (c, d, and e) 5.0 and (f, g, and h) 10.0 mM under pH. 5.0 for (c, f) 6, (d, g) 12, and (e, h) 48 h.

GSH concentrations higher than that in normal tissues (at least 4-fold increase). Therefore, the biodegradation behaviors of Mn-HMSNs under different reducing microenvironments were then investigated. Similar to pH influence, the presence of GSH could also accelerate the releasing of Mn and Si from the carrier; that is, the biodegradation is GSH concentration-dependent (Figure 5a,b). TEM image shows that the nano/meso-structure of Mn-HMSNs has quickly broken up in SBF solution containing GSH only within 6 h. Importantly, the structure has collapsed and fused with each other after long-term biodegradation of Mn-HMSNs in GSH solution (Figure 5c–h). Therefore, this result also provides the direct evidence of GSH-dependent biodegradation behavior of Mn-HMSNs where reducing microenvironment can accelerate the biodegradation of Mn-HMSNs.

Furthermore, the biodegradation behavior of Mn-HMSNs under the concurrent acidic (pH. 5.0) and reducing conditions ([GSH] = 5.0 and 10.0 mM) were also assessed. It can be found that the releasing rates of Mn (Figure 6a) and Si (Figure 6b) under such a combinatorial condition are much higher than the biodegradation in either acidic or reducing condition. The structural evolution was further probed by TEM characterization at different stages of biodegradation, which exhibited that the structure of Mn-HMSNs collapsed quickly in the combined acidic and reducing conditions (Figure 6c–h). Comparatively, the biodegradation of traditional MSNs with rigid Si–O–Si framework shows much slower biodegradation and structural collapse under either acidic or reducing condition (Figure S2), showing the advantage of Mn doping in tuning the biodegradability of silica framework. Furthermore, the structural evolution during the biodegradation of Mn-HMSNs was observed by SEM where the significant structural collapse of Mn-HMSNs was observed (Figure S3), consistent with the aforementioned TEM observations.

It is still difficult to reveal the intracellular biodegradation behavior of silica-based nanocarriers. Herein we introduced bio-TEM to directly observe the structural evolution of Mn-HMSNs after the uptake by cancer cells for varied durations (1, 2, 3, and 7 d). As shown in Figure 7, Mn-HMSNs can be easily endocytosized into cancer cells and accumulate into the cytoplasm of cells at the initial stage (Figure 7a–c). Importantly, the fast biodegradation of Mn-HMSNs is clearly shown in bio-TEM images only in 48 h intracellular uptake (Figure 7d–f), as revealed by the cloudy morphology without defined spherical structure. In 3 d intracellular biodegradation, it was found that the biodegradation resulted in significant fusion of degraded products (Figure 7g–i). It should be noted that the observed degradation residues in the TEM are only a very small fraction of degradation products, most of them are small molecules remaining in the solutions. After prolonged incubation, no significant material formulations could be found intracellularly after 7 d biodegradation (Figure 7j–l), demonstrating that the biodegraded species could be easily excreted out of the cells. The bio-TEM observation of intracellular biodegradation results of Mn-HMSNs is in consistence with the biodegradation assay in SBF under different conditions (e.g., varied pHs and GSH concentrations), thus it is concluded that the intracellular mild acidic condition and reducing microenvironment of cancer cells can fast trigger the breakup of this composite inorganic nanosystem and subsequent biodegradation and excretion out of the cancer cells/tumor tissues.

3.3. Theranostic Functions of Mn-HMSNs Sensitive to Tumor Microenvironment. Such a tumor microenvironment-triggered biodegradation behavior of Mn-HMSNs could exert the specific functions for theranostic applications. To facilitate the biomedical applications, the colloidal stability of Mn-HMSNs in physiological condition was improved by the typical PEGylation (designated as PEG/Mn-HMSNs). Because of the presence of paramagnetic Mn centers, the contrast-enhanced MRI capability was initially evaluated at different pHs and GSH concentrations. The initial longitudinal relaxivity r_1 of PEG/Mn-HMSNs in neutral SBF was as low as 0.51 mM^{-1} s^{-1} but increased substantially to 0.83 and 2.46 mM^{-1} s^{-1} at GSH concentrations of 5.0 and 10.0 mM (Figure 8a), respectively. Such a contrast-enhanced responsiveness was also realized in

DOI: 10.1021/jacs.6b04299
J. Am. Chem. Soc. 2016, 138, 9881–9894

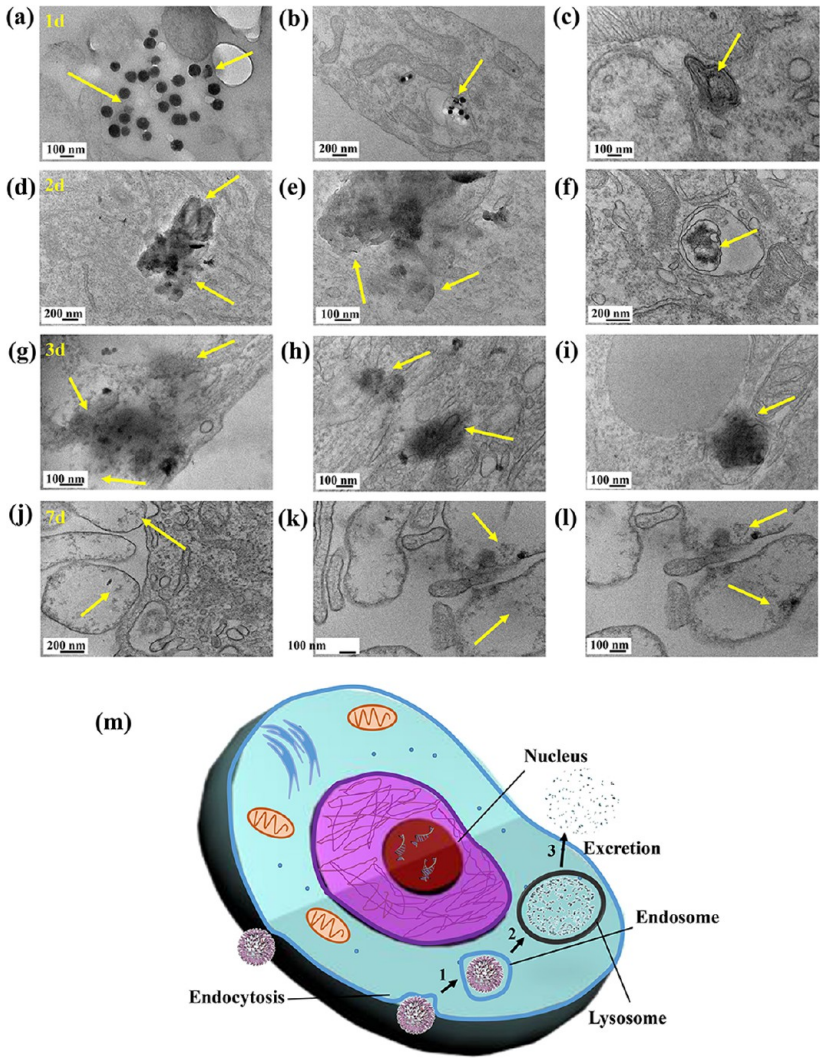

Figure 7. Bio-TEM images of cells after coincubation with Mn-HMSNs to observe the intracellular biodegradation behavior of Mn-HMSNs. The coincubation duration included (a–c) 1, (d–f) 2, (g–i) 3, and (j–l) 7 d, respectively. (m) Schematic illustration intracellular biodegradation of Mn-HMSNs.

mild acidic condition (pH 5.0) where r_1 also gained a substantial increment (Figure 8b). The enhancement of T_1 signal is accompanied by the improvement of T_2 signals (Figure 8e,f), which can be clearly observed in phantom images of corresponding SBF solutions (Figure 8c, d, g, and h). Such a unique pH- and GSH-responsive MRI performance is due to the fast biodegradation of PEG/Mn-HMSNs, which enhances the interaction probability of Mn paramagnetic centers with water molecules.[64] Therefore, PEG/Mn-HMSNs can act as the desirable responsive contrast agents for MR imaging sensitive to tumor-specific microenvironment. In vivo MR imaging of tumor-bearing mice was conducted by intravenous administration of PEG/Mn-HMSNs at a low PEG/Mn-HMSNs dose of 5 mg/kg. It can be found that the positive MRI signal is significantly enhanced after the injection of PEG/Mn-HMSNs, owing to the enhanced permeability and retention (EPR) effect of tumor for the tumor accumulation of PEG/Mn-HMSNs (Figure 8i), as further demonstrated by the continuous enhancements of the MRI-signal intensities (Figure 8j).

Such a unique "manganese extraction" strategy and biodegradation behavior of Mn-HMSNs can fast trigger the releasing of anticancer drugs, establishing a novel biodegradation-triggered stimuli-responsive drug-releasing pattern.[68,69] As a paradigm, anticancer drug doxorubicin (DOX) was loaded into PEG/Mn-HMSNs with concurrent high drug-loading efficiency (78%) and capacity (16%). In vitro drug-releasing profiles were recorded by immersing DOX-loaded PEG/Mn-HMSNs into SBF solutions of different GSH concentrations ([GSH] = 5.0 and 10.0 mM). It can be found that the DOX-releasing in pure SBF solution is slow, but the releasing rate increases quickly in SBF solutions containing GSH. The 48 h-releasing in pure SBF is as low as 8.9%, which, however, increases to 27% and 37% at GSH concentrations of 5.0 and 10.0 mM, respectively (Figure 9a). Importantly, such a responsive drug-releasing profile was also achieved in SBF solutions at different pHs where mild acidic SBF solution enabled the quick drug releasing (Figure 9b). Further, the drug releasing shows much enhanced rates in concurrent acidic and reducing conditions because of the fast biodegradation rate of the nanocarriers (Figure 9c). It is noted that this biodegradation-triggered drug-releasing modality is much favorable for anticancer drug releasing (Figure 9d). On one hand, the present strategy is very facile as the tedious construction of special nanovalves onto the surface of

DOI: 10.1021/jacs.6b04299
J. Am. Chem. Soc. 2016, 138, 9881–9894

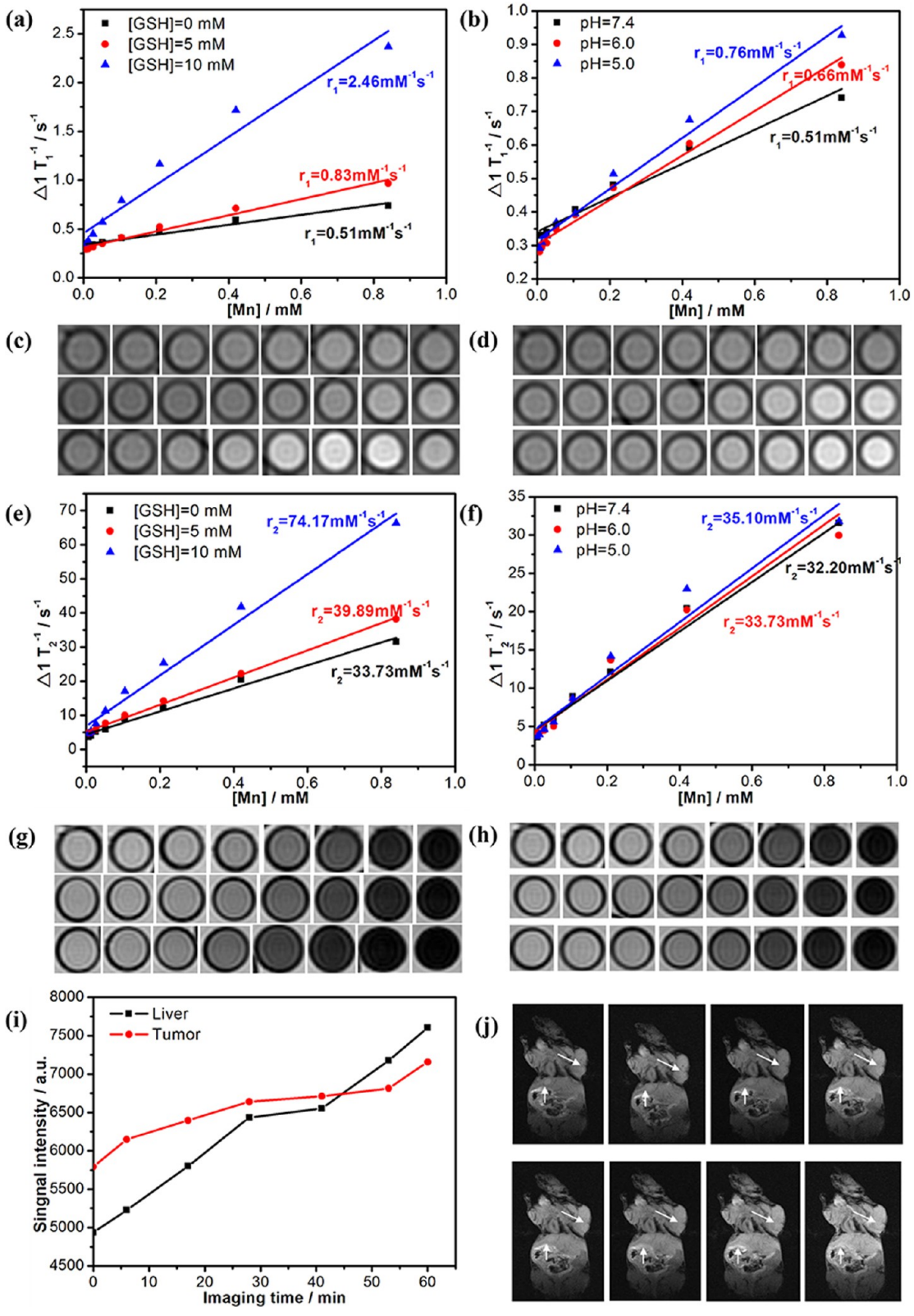

Figure 8. (a) $\Delta 1/T_1$ versus Mn concentration for PEG/Mn-HMSNs SBF solution (black lines) and PEG/Mn-HMSNs SBF solution at varied GSH concentrations (red lines for [GSH] = 5.0 mM, blue lines for [GSH] = 10.0 mM), and (b) at varied pHs (red line for pH = 6.0, blue line for pH = 5.0). (c) T_1-weighted MR imaging of PEG/Mn-HMSNs in SBF at varied GSH concentrations and (d) at varied pHs. (e) $\Delta 1/T_2$ versus Mn concentration for PEG/Mn-HMSNs SBF solution (black line), PEG/Mn-HMSNs SBF solution at varied GSH concentrations, and (f) at varied pHs. (g) T_2-weighted MRI results of PEG/Mn-HMSNs in SBF at varied GSH concentrations and (h) at varied pHs. (i) The MRI-signal intensity of (j) corresponding in vivo T_1-weighted MR imaging of tumor-bearing mice after intravenous administration of PEG/Mn-HMSNs and the quantitative signal intensities of liver and tumor. Arrows in j indicate the tumor tissue.

DOI: 10.1021/jacs.6b04299
J. Am. Chem. Soc. 2016, 138, 9881−9894

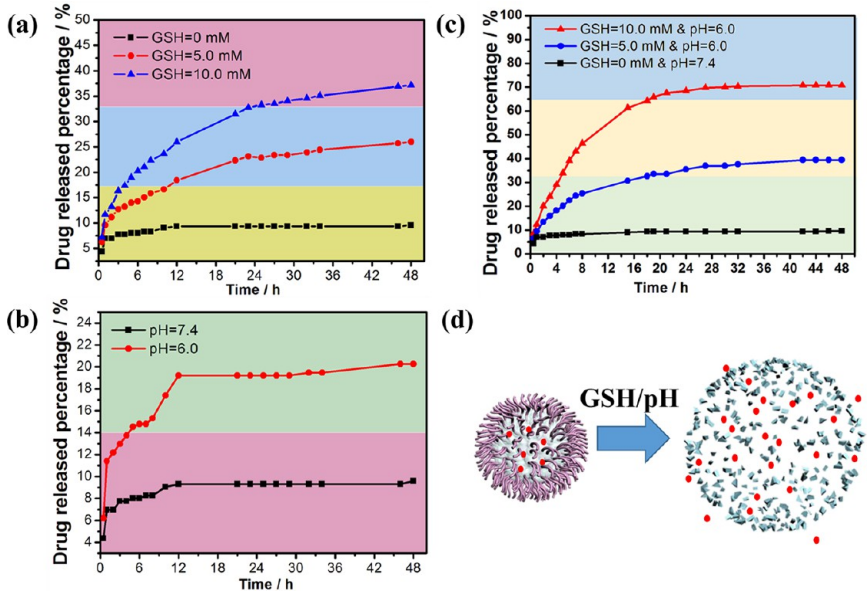

Figure 9. In vitro DOX-releasing profiles from DOX-PEG/Mn-HMSNs in SBF at (a) elevated GSH concentrations, (b) varied pHs, and (c) combined acidic/reducing conditions. (d) Schematic illustration of DOX-releasing profiles from DOX-PEG/Mn-HMSNs accompanying the biodegradation process.

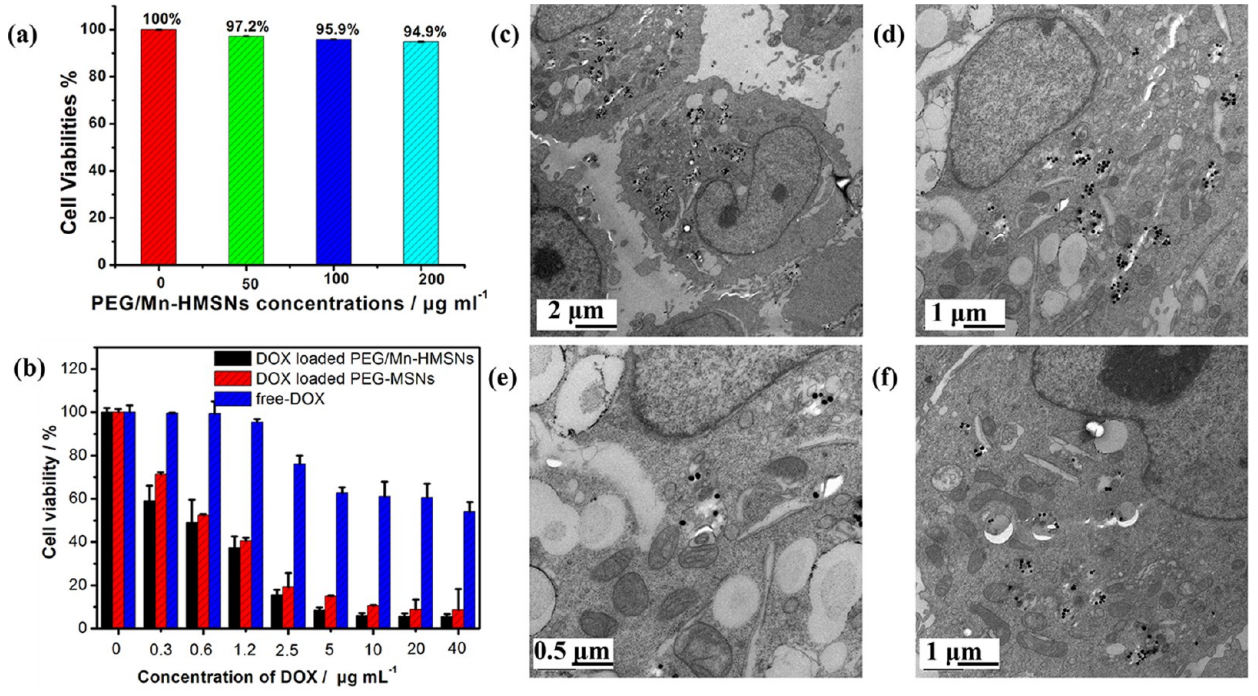

Figure 10. (a) Cell viabilities of Hep G2 cells after the coincubation with Mn-HMSNs, (b) cytotoxicity of DOX-loaded PEG/Mn-HMSNs, DOX-loaded PEG/MSNs, and free DOX against Hep G2 cells. (c–f) Bio-TEM images of Hep G2 cells after the coincubation with Mn-HMSNs at different magnifications for 1 d.

mesopores for on-demand drug releasing becomes unnecessary; On the other hand, the biodegradation-triggered drug releasing could enable the concurrent therapeutics by drug releasing, enhanced MR imaging and excretion by the biodegradation.

A typical MTT method was used to assess the in vitro cytotoxicity of PEG/Mn-HMSNs. As Figure 10a shows, the cell viability of Hep G2 cells still maintains at 94.9% even after coincubation with PEG/Mn-HMSNs at a high concentration of 200 μg/mL, indicating that blank PEG/Mn-HMSNs is low-toxic. Compared to the equivalent concentrations of free DOX, the cells coincubated with DOX-loaded PEG/Mn-HMSNs show much lower viabilities (Figure 10b), showing that the delivery of DOX mediated by PEG/Mn-HMSNs can bring with substantially enhanced therapeutic efficacy of DOX against Hep G2 cancer cells. In addition, DOX-loaded PEG/Mn-HMSNs exhibit higher cytotoxicity compared to that of DOX-loaded MSNs, which could be attributed to the fast intracellular biodegradation of PEG/Mn-HMSNs to trigger the DOX releasing and enhance therapeutic efficacy. Bio-TEM results exhibit that large amounts of PEG/Mn-HMSNs can enter the

DOI: 10.1021/jacs.6b04299
J. Am. Chem. Soc. 2016, 138, 9881–9894

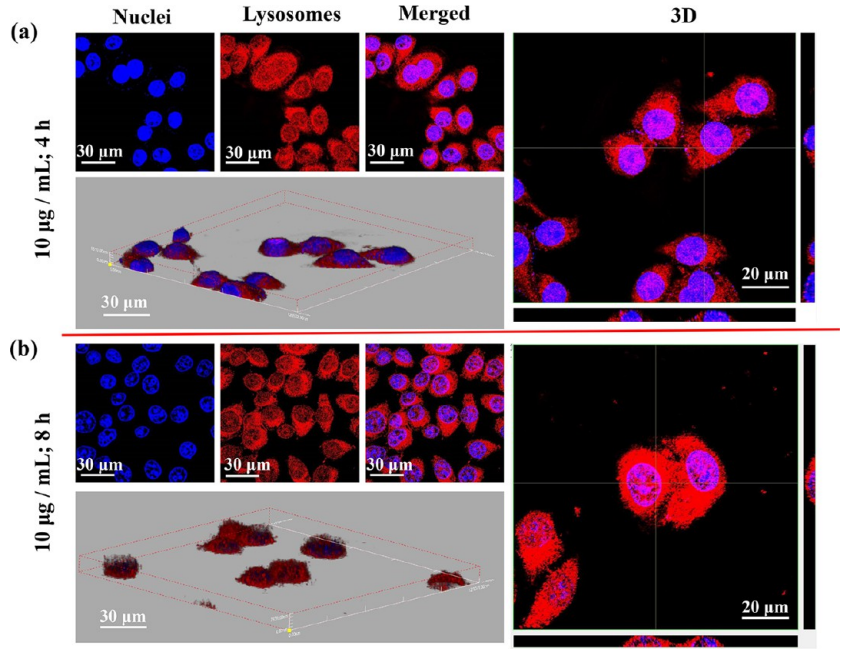

Figure 11. CLSM images of Hep G2 cells after coincubation with DOX-loaded Mn-HMSNs ([DOX] = 10 μg/mL) for (a) 4 h and (b) 8 h.

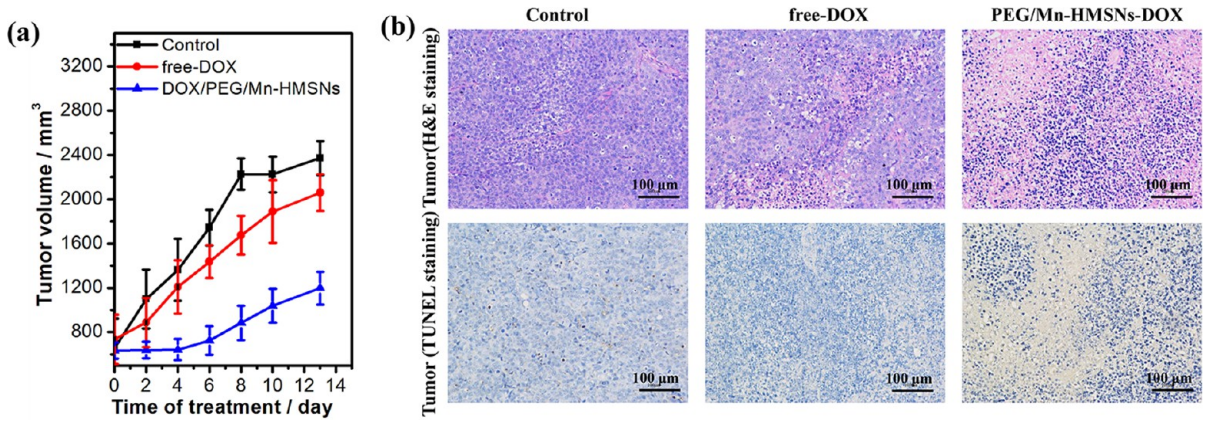

Figure 12. (a) Tumor-growth inhibition effect by different treatments as shown in the figure and (b) histological assessments from the tumors borne in mice treated with saline (control), free DOX (2.5 mg/kg), and DOX@PFG/Mn-HMSNs at the equivalent DOX dose of 2.5 mg/kg.

cancer cells and accumulate into the cytoplasm (Figure 10c–f), guaranteeing the subsequent intracellular transport of anticancer drugs. Furthermore, confocal laser scanning microscopy (CLSM) was used to observe the uptake of DOX-loaded Mn-HMSNs and their intracellular DOX-releasing behavior based on the intrinsic red fluorescence of DOX. As shown in Figure 11, high-intensity red fluorescence representing DOX molecules are found in nucleus of cancer cells, indicating that PEG/Mn-HMSNs can efficiently deliver and release DOX intracellularly, which is also time-dependent. The intracellular accumulation of DOX-loaded PEG/Mn-HMSNs was further demonstrated by three-dimensional (3D) fluorescence reconstruction of *Z*-axis-scanned CLSM images (Figure S4 and S5) where DOX-loaded PEG/Mn-HMSNs could be clearly found around the nuclei of cancer cells (Figure 11). The in vitro cytotoxicity assay and CLSM observation demonstrated that PEG/Mn-HMSNs could efficiently deliver anticancer into cancer cells to exert high therapeutic functionality against cancer cells.

The encouraging in vitro therapeutic outcome potentially ensures highly promising *in vivo* therapeutic indexes. Hep G2 tumor xenograft was established on Balb/c nude mice for further *in vivo* therapeutic assay. The therapeutic outcome was evaluated by intravenous administration of free DOX and DOX-loaded PEG/Mn-HMSNs at a low equivalent DOX dose of 2.5 mg/kg. The tumor volume was recorded at given time interval. As shown in Figure 12a, the intravenous administration of DOX-loaded PEG/Mn-HMSNs has significantly inhibited the tumor growth while the same free DOX dose shows much weaker tumor-inhibition effect at the low DOX dose. Such a high tumor-inhibition effect is due to the enhanced accumulation of DOX-loaded PEG/Mn-HMSNs within tumor and fast biodegradation-promoted DOX releasing from the carrier triggered by mild acidic/reducing tumor microenvironment. TUNEL (TdT-mediated dUTP Nick-End Labeling) and H&E (Hematoxylin-Eosin staining) staining results showed the strong necrosis of tumor cells after the treatment with DOX-loaded PEG/Mn-HMSNs compared to the mice treated with free DOX (Figure 12b). Importantly, the DOX

DOI: 10.1021/jacs.6b04299
J. Am. Chem. Soc. 2016, 138, 9881–9894

delivery mediated by PEG/Mn-HMSNs resulted in decreased DOX cytotoxicity to normal organs, while free DOX would cause the significant damages to liver, heart, kidney and spleen, as clearly demonstrated by H&E staining results for pathological assessment (Figure 13).

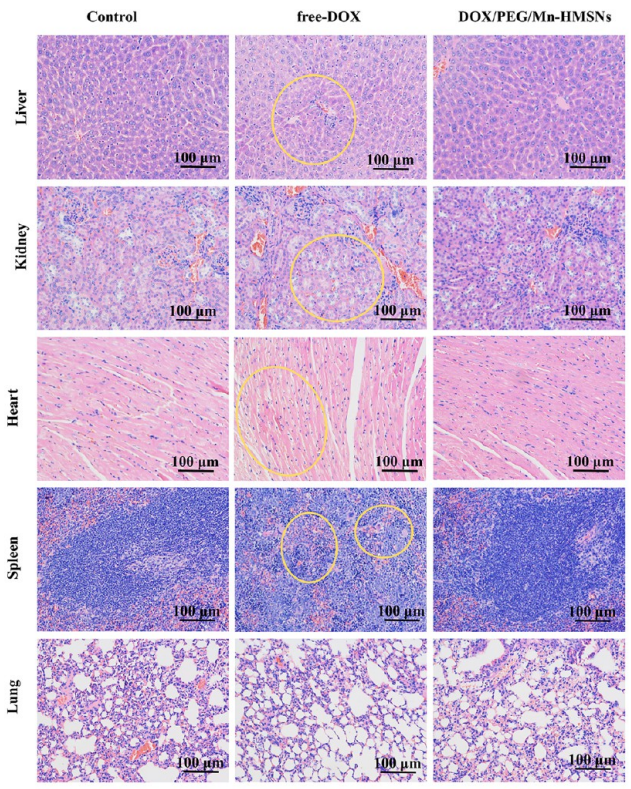

Figure 13. Histological assessments for the major organs (liver, kidney, heart, spleen, and lung) of tumor-bearing mice after the treatment with saline (control), free-DOX, and DOX@PFG/Mn-HMSNs at the equivalent DOX dose of 2.5 mg/kg.

Furthermore, we conducted the in vivo biodistribution evaluation and excretion assessment after the intravenous administration of PEG/Mn-HMSNs into tumor-bearing mice (Figure S6). Conventional MSNs were used as the comparison counterpart. It was found that the accumulation amount of PEG/Mn-HMSNs in major organs decreased significantly with the prolonged feeding time. In addition, PEG/Mn-HMSNs could be quickly excreted out of the body via the faeces and urines. Compared to conventional MSNs, PEG/Mn-HMSNs showed enhanced Si excretion amounts in urine because of the quick biodegradation of PEG/Mn-HMSNs, which produced small molecular biodegradation products that could be easily excreted via urine route.

3.4. In Vivo Biocompatibility Evaluation of PEG/Mn-HMSNs. To facilitate the potential clinical translation of PEG/Mn-HMSNs, their in vivo biocompatibility was assessed by intravenous administration into healthy mice at elevated doses (0, 5, 10, and 20 mg/kg). The body weight of mice was recorded every 2 days and during one-month feeding. Then, the mice were sacrificed and the histocompatibility was evaluated by H&E staining. From the body weight of mice changing curves (Figure S7), it can be found that there are no significant differences in weight change between the control group and PEG/Mn-HMSNs-treated groups. In addition, the tissues of major organs have no obvious pathological abnormity compared to control mice, showing high histocompatibility of PEG/Mn-HMSNs (Figure S8). In addition, the liver-function indexes and major blood indexes of mice after receiving PEG/Mn-HMSNs at different doses also show no significant difference and abnormity compared to control mice, further demonstrating the high biocompatibility of PEG/Mn-HMSNs (Figure S9).

4. CONCLUSIONS

In summary, biodegradable transition-metal Mn-doped hollow MSNs has been developed as a novel theranostic platform for tumor microenvironment-sensitive biodegradation and theranostics of cancer. Mn-HMSNs with a large hollow interior and unique nanospheres-assembled mesoporous shell were constructed by the topological transformation of traditional MSNs into Mn-doped hollow MSNs under hydrothermal conditions. Such a "metal ion-doping" approach enables the accelerated biodegradation of Mn-HMSNs in either mild acidic or reducing microenvironment by breaking up the Mn−O bond and subsequent triggering "manganese extraction", which further accelerates the biodegradation of Si−O−Si bonds. This is the first demonstration of biodegradable inorganic mesoporous nanosystems with specific biodegradation behavior sensitive to tumor microenvironment. Importantly, the fast biodegradation of Mn-HMSNs has promoted the anticancer drug releasing and enhanced T_1-weighted MR imaging, as systematically demonstrated both in vitro and in vivo. High tumor-inhibition effect has been also achieved by anticancer drug delivery mediated by PEGylated Mn-HMSNs. Therefore, this research provides a novel approach to realize the on-demand biodegradation of inorganic nanomaterials and tumor-sensitive theranostic functions, which is expected to pave a new way to solve the critical low biodegradation issue of inorganic material nano-family.

■ ASSOCIATED CONTENT

Supporting Information

The Supporting Information is available free of charge on the ACS Publications website at DOI: 10.1021/jacs.6b04299.

Experimental details, additional characterization data for Mn-HMSNs and intracellular uptake, and in vivo biocompatibility of Mn-HMSNs (PDF)

■ AUTHOR INFORMATION

Corresponding Authors

*chenyu@mail.sic.ac.cn
*hrchen@mail.sic.ac.cn
*jlshi@mail.sic.ac.cn

Notes

The authors declare no competing financial interest.

■ ACKNOWLEDGMENTS

We acknowledge financial supports from China National Funds for Distinguished Young Scientists (Grant No. 51225202). The National Nature Science Foundation of China (Grant Nos. 51302293 and 51132009), Natural Science Foundation of Shanghai (13ZR1463500), Shanghai Rising-Star Program (14QA1404100), and Shanghai Excellent Academic Leaders Program (14XD1403800) are also acknowledged.

DOI: 10.1021/jacs.6b04299
J. Am. Chem. Soc. 2016, 138, 9881−9894

REFERENCES

(1) Peer, D.; Karp, J. M.; Hong, S.; FarokHzad, O. C.; Margalit, R.; Langer, R. *Nat. Nanotechnol.* **2007**, *2*, 751.
(2) Mura, S.; Nicolas, J.; Couvreur, P. *Nat. Mater.* **2013**, *12*, 991.
(3) Ashley, C. E.; Carnes, E. C.; Phillips, G. K.; Padilla, D.; Durfee, P. N.; Brown, P. A.; Hanna, T. N.; Liu, J.; Phillips, B.; Carter, M. B.; Carroll, N. J.; Jiang, X.; Dunphy, D. R.; Willman, C. L.; Petsev, D. N.; Evans, D. G.; Parikh, A. N.; Chackerian, B.; Wharton, W.; Peabody, D. S.; Brinker, C. J. *Nat. Mater.* **2011**, *10*, 389.
(4) He, Q. J.; Shi, J. L. *J. Mater. Chem.* **2011**, *21*, 5845.
(5) Stark, W. J. *Angew. Chem., Int. Ed.* **2011**, *50*, 1242.
(6) Allen, T. M.; Cullis, P. R. *Science* **2004**, *303*, 1818.
(7) Liong, M.; Lu, J.; Kovochich, M.; Xia, T.; Ruehm, S. G.; Nel, A. E.; Tamanoi, F.; Zink, J. I. *ACS Nano* **2008**, *2*, 889.
(8) Lee, J. E.; Lee, N.; Kim, H.; Kim, J.; Choi, S. H.; Kim, J. H.; Kim, T.; Song, I. C.; Park, S. P.; Moon, W. K.; Hyeon, T. *J. Am. Chem. Soc.* **2010**, *132*, 552.
(9) Della Rocca, J.; Liu, D.; Lin, W. *Acc. Chem. Res.* **2011**, *44*, 957.
(10) Zhao, Y.; Trewyn, B. G.; Slowing, II; Lin, V. S. *J. Am. Chem. Soc.* **2009**, *131*, 8398.
(11) Meng, F.; Cheng, R.; Deng, C.; Zhong, Z. *Mater. Today* **2012**, *15*, 436.
(12) Song, Y. Y.; Schmidt-Stein, F.; Bauer, S.; Schmuki, P. *J. Am. Chem. Soc.* **2009**, *131*, 4230.
(13) Huang, X. H.; El-Sayed, I. H.; Qian, W.; El-Sayed, M. A. *J. Am. Chem. Soc.* **2006**, *128*, 2115.
(14) Boisselier, E.; Astruc, D. *Chem. Soc. Rev.* **2009**, *38*, 1759.
(15) Ma, M.; Chen, H.; Chen, Y.; Wang, X.; Chen, F.; Cui, X.; Shi, J. *Biomaterials* **2012**, *33*, 989.
(16) Kim, M.; Sohn, K.; Bin Na, H.; Hyeon, T. *Nano Lett.* **2002**, *2*, 1383.
(17) Hu, Y.; Chen, Q.; Ding, Y.; Li, R.; Jiang, X.; Liu, B. *Adv. Mater.* **2009**, *21*, 3639.
(18) Chen, J.; Guo, Z.; Wang, H. B.; Gong, M.; Kong, X. K.; Xia, P.; Chen, Q. W. *Biomaterials* **2013**, *34*, 571.
(19) Kam, N. W. S.; O'Connell, M.; Wisdom, J. A.; Dai, H. J. *Proc. Natl. Acad. Sci. U. S. A.* **2005**, *102*, 11600.
(20) Losic, D.; Simovic, S. *Expert Opin. Drug Delivery* **2009**, *6*, 1363.
(21) Bae, C.; Yoo, H.; Kim, S.; Lee, K.; Kim, J.; Sung, M. A.; Shin, H. *Chem. Mater.* **2008**, *20*, 756.
(22) Kim, T. W.; Chung, P. W.; Slowing, I. I.; Tsunoda, M.; Yeung, E. S.; Lin, V. S. Y. *Nano Lett.* **2008**, *8*, 3724.
(23) Hao, R.; Xing, R.; Xu, Z.; Hou, Y.; Gao, S.; Sun, S. *Adv. Mater.* **2010**, *22*, 2729.
(24) Zhu, Y.; Ikoma, T.; Hanagata, N.; Kaskel, S. *Small* **2010**, *6*, 471.
(25) Cao, S. W.; Zhu, Y. J.; Ma, M. Y.; Li, L.; Zhang, L. *J. Phys. Chem. C* **2008**, *112*, 1851.
(26) Gao, X.; Cui, Y.; Levenson, R. M.; Chung, L. W.; Nie, S. *Nat. Biotechnol.* **2004**, *22*, 969.
(27) Rosenholm, J. M.; Mamaeva, V.; Sahlgren, C.; Linden, M. *Nanomedicine (London, U. K.)* **2012**, *7*, 111.
(28) Li, Z.; Barnes, J. C.; Bosoy, A.; Stoddart, J. F.; Zink, J. I. *Chem. Soc. Rev.* **2012**, *41*, 2590.
(29) Wu, S.-H.; Hung, Y.; Mou, C.-Y. *Chem. Commun.* **2011**, *47*, 9972.
(30) Zhao, D.; Feng, J.; Huo, Q.; Melosh, N.; Fredrickson, G. H.; Chmelka, B. F.; Stucky, G. D. *Science* **1998**, *279*, 548.
(31) Sun, Z.; Deng, Y.; Wei, J.; Gu, D.; Tu, B.; Zhao, D. *Chem. Mater.* **2011**, *23*, 2176.
(32) Fowler, C. E.; Khushalani, D.; Mann, S. *Chem. Commun.* **2001**, 2028.
(33) Zhu, Y.; Shi, J.; Shen, W.; Dong, X.; Feng, J.; Ruan, M.; Li, Y. *Angew. Chem.* **2005**, *117*, 5213.
(34) Pan, L.; He, Q.; Liu, J.; Chen, Y.; Ma, M.; Zhang, L.; Shi, J. *J. Am. Chem. Soc.* **2012**, *134*, 5722.
(35) Liu, J.; Bu, W.; Pan, L.; Shi, J. *Angew. Chem., Int. Ed.* **2013**, *52*, 4375.
(36) He, Q.; Shi, J.; Chen, F.; Zhu, M.; Zhang, L. *Biomaterials* **2010**, *31*, 3335.
(37) Wu, H.; Liu, G.; Zhang, S.; Shi, J.; Zhang, L.; Chen, Y.; Chen, F.; Chen, H. *J. Mater. Chem.* **2011**, *21*, 3037.
(38) Slowing, I. I.; Trewyn, B. G.; Giri, S.; Lin, V. S. Y. *Adv. Funct. Mater.* **2007**, *17*, 1225.
(39) Gao, Y.; Chen, Y.; Ji, X.; He, X.; Yin, Q.; Zhang, Z.; Shi, J.; Li, Y. *ACS Nano* **2011**, *5*, 9788.
(40) Chen, Y.; Chen, H.; Zeng, D.; Tian, Y.; Chen, F.; Feng, J.; Shi, J. *ACS Nano* **2010**, *4*, 6001.
(41) Zhao, W.; Gu, J.; Zhang, L.; Chen, H.; Shi, J. *J. Am. Chem. Soc.* **2005**, *127*, 8916.
(42) Chen, Y.; Chen, H.; Guo, L.; He, Q.; Chen, F.; Zhou, J.; Feng, J.; Shi, J. *ACS Nano* **2010**, *4*, 529.
(43) Slowing, II; Vivero-Escoto, J. L.; Wu, C. W.; Lin, V. S. *Adv. Drug Delivery Rev.* **2008**, *60*, 1278.
(44) Lu, J.; Liong, M.; Li, Z.; Zink, J. I.; Tamanoi, F. *Small* **2010**, *6*, 1794.
(45) Tang, F.; Li, L.; Chen, D. *Adv. Mater.* **2012**, *24*, 1504.
(46) He, Q.; Shi, J. *J. Mater. Chem.* **2011**, *21*, 5845.
(47) Pohaku Mitchell, K. K.; Liberman, A.; Kummel, A. C.; Trogler, W. C. *J. Am. Chem. Soc.* **2012**, *134*, 13997.
(48) Peng, Y. K.; Tseng, Y. J.; Liu, C. L.; Chou, S. W.; Chen, Y. W.; Tsang, S. C.; Chou, P. T. *Nanoscale* **2015**, *7*, 2676.
(49) Zhang, S.; Chu, Z.; Yin, C.; Zhang, C.; Lin, G.; Li, Q. *J. Am. Chem. Soc.* **2013**, *135*, 5709.
(50) Li, J.; Zhao, Z.; Feng, J.; Gao, J.; Chen, Z. *Nanotechnology* **2013**, *24*, 455102.
(51) Chen, Y.; Ye, D.; Wu, M.; Chen, H.; Zhang, L.; Shi, J.; Wang, L. *Adv. Mater.* **2014**, *26*, 7019.
(52) Loving, G. S.; Mukherjee, S.; Caravan, P. *J. Am. Chem. Soc.* **2013**, *135*, 4620.
(53) Pautler, R. G.; Silva, A. C.; Koretsky, A. P. *Magn. Reson. Med.* **1998**, *40*, 740.
(54) Silva, A. C.; Lee, J. H.; Aoki, I.; Koretsky, A. P. *NMR Biomed.* **2004**, *17*, 532.
(55) Chen, Y.; Yin, Q.; Ji, X.; Zhang, S.; Chen, H.; Zheng, Y.; Sun, Y.; Qu, H.; Wang, Z.; Li, Y.; Wang, X.; Zhang, K.; Zhang, L.; Shi, J. *Biomaterials* **2012**, *33*, 7126.
(56) Jun, Y. W.; Lee, J. H.; Cheon, J. *Angew. Chem., Int. Ed.* **2008**, *47*, 5122.
(57) Deng, R.; Xie, X.; Vendrell, M.; Chang, Y. T.; Liu, X. *J. Am. Chem. Soc.* **2011**, *133*, 20168.
(58) Zhao, Z.; Fan, H.; Zhou, G.; Bai, H.; Liang, H.; Wang, R.; Zhang, X.; Tan, W. *J. Am. Chem. Soc.* **2014**, *136*, 11220.
(59) Bhang, S. H.; Han, J.; Jang, H. K.; Noh, M. K.; La, W. G.; Yi, M.; Kim, W. S.; Kwon, Y. K.; Yu, T.; Kim, B. S. *Biomaterials* **2015**, *55*, 33.
(60) Wen, H. Y.; Dong, H. Q.; Xie, W. J.; Li, Y. Y.; Wang, K.; Pauletti, G. M.; Shi, D. L. *Chem. Commun.* **2011**, *47*, 3550.
(61) Liotta, L. A.; Kohn, E. C. *Nature* **2001**, *411*, 375.
(62) Lin, Y.-S.; Hurley, K. R.; Haynes, C. L. *J. Phys. Chem. Lett.* **2012**, 364.
(63) Rosenholm, J. M.; Mamaeva, V.; Sahlgren, C.; Linden, M. *Nanomedicine* **2012**, *7*, 111.
(64) Kim, T.; Momin, E.; Choi, J.; Yuan, K.; Zaidi, H.; Kim, J.; Park, M.; Lee, N.; McMahon, M. T.; Quinones-Hinojosa, A.; Bulte, J. W. M.; Hyeon, T.; Gilad, A. A. *J. Am. Chem. Soc.* **2011**, *133*, 2955.
(65) Yec, C. C.; Zeng, H. C. *ACS Nano* **2014**, *8*, 6407.
(66) Zhan, G.; Yec, C. C.; Zeng, H. C. *Chem. - Eur. J.* **2015**, *21*, 1882.
(67) Wang, Y.; Wang, G.; Wang, H.; Liang, C.; Cai, W.; Zhang, L. *Chem. - Eur. J.* **2010**, *16*, 3497.
(68) Liu, R.; Zhang, Y.; Zhao, X.; Agarwal, A.; Mueller, L. J.; Feng, P. Y. *J. Am. Chem. Soc.* **2010**, *132*, 1500.
(69) Lai, C. Y.; Trewyn, B. G.; Jeftinija, D. M.; Jeftinija, K.; Xu, S.; Jeftinija, S.; Lin, V. S. *J. Am. Chem. Soc.* **2003**, *125*, 4451.

DOI: 10.1021/jacs.6b04299
J. Am. Chem. Soc. 2016, 138, 9881−9894